NUMERICAL ANALYSIS OF TURBULENT FLOW IN A CONICAL DIFFUSER

K. K. Adane, M. F. Tachie, and S. J. Ormiston
University of Manitoba, Winnipeg, Canada
Email: tachiemf@cc.umanitoba.ca

Received July 2005, Accepted August 2006
No. 05-CSME-24, E.I.C. Accession 2876

ABSTRACT

A commercial CFD code, CFX-TASCflow, is used to predict turbulent flow in a conical diffuser. The computation was performed using a low-Reynolds number k–ε model, low-Reynolds number k–ω model, a low-Reynolds number k–ω based non-linear algebraic Reynolds stress model, and a second moment closure with a wall-function. The experimental datasets of Singh [1] and Kassab [2] are used to validate the numerical results. The results show that all the turbulence models reproduce the static pressure coefficient distribution reasonably well. The low Reynolds number k–ω models give better prediction of the friction velocity than the second moment closure. The models also predict the Reynolds shear stress reasonably well but fail to reproduce the correct level of the kinetic energy.

ANALYSE NUMERIQUE D'UN ECOULEMENT TURBULENT DANS UN DIFFUSEUR CONIQUE

RÉSUMÉ

Un code commercial de CFD, CFX-TASCflow, a été utilisé pour la modélisation des écoulements turbulents dans un diffuseur conique. Les calculs étaient effectués en utilisant les quatre modèles de la turbulence suivants : k–ε et k–ω pour des bas nombres de Reynolds, k–ω pour des bas nombres de Reynolds mais basé sur un modèle non linéaire des contraintes de Reynolds, et enfin un modèle du second ordre avec une fonction de parois standard. Les calculs étaient validés par une comparaison avec les résultats expérimentaux de Singh [1] et de Kassab [2]. Cette comparaison a montré que tous ces modèles de turbulence ont donné de bon résultat pour la distribution du coefficient de la pression statique. En plus, les modèles k–ω pour des bas nombres de Reynolds ont prévu la vitesse de friction mieux que le modèle du second ordre. Enfin, tous ces modèles ont donné de bon résultat concernant les contraintes de cisaillement, mais ils se sont montrés incapables de produire le vrai niveau de l'énergie cinétique.

1.0 INTRODUCTION

Turbulent diffuser flows are found in numerous fluid engineering applications, such as in HVAC systems and in the draft tube of a hydro power plant. In these and many other applications, the basic goal of the diffuser is to convert the mean kinetic energy into pressure energy, thereby producing an adverse pressure gradient in the flow direction. The combined effects of adverse pressure gradient and streamwise curvature may significantly increase the complexity of the transport phenomena in the diffuser in comparison to turbulent flows in a pipe. For example, if the adverse pressure gradient is strong, the flow may separate and the classical logarithmic velocity profile is not valid. Prior experimental results clearly demonstrate that the peak values of the turbulent kinetic energy and Reynolds shear stress, and the distribution of dissipation length scale are significantly higher in a turbulent diffuser than in pipe flows (Azad and Kassab [3]). Adverse pressure gradient also has significant effects on the transport terms (e.g., production, dissipation and diffusion) in the turbulent kinetic energy equation. These complex features pose significant challenges to the ability of standard near-wall turbulence models to predict turbulent diffuser flows.

Given their practical importance and complexity from viewpoint of fundamental turbulence research, turbulent diffuser flows have been the focus of numerous prior experimental and numerical studies. The conical diffuser has been studied quite extensively, for example, by Arora and Azad [4] and Trupp *et al.* [5]. The results obtained from these and other experiments have improved our physical understanding of the effects of adverse pressure gradient on the turbulence structure. The experimental results have also been used in the past to evaluate the ability of various near-wall turbulence models to predict turbulent flow in conical diffusers (Lai *et al.* [6]; Cho and Fletcher [7]).

The focus of this paper is to apply a commercial CFD code, CFX-TASCflow, and turbulence models of varying sophistication and different near-wall treatment to predict turbulent conical diffuser flow. A schematic of the flow geometry and coordinate system are shown in Figure 1. The inlet pipe to the diffuser is $64D_i$ long and has a diameter $D_i = 0.1016$ m. The diffuser has a total divergence angle of 8° and an area ratio of 4:1 over its total length of $7.09D_i$ and $7.33D_i$.

The geometry shown in Figure 1 has been studied at various Reynolds numbers at the University of Manitoba. The results of Trupp *et al.* [5] at Re = 115,000 were used in the numerical investigation of Lai *et al* [6]. The computation was performed using a k-ε model with

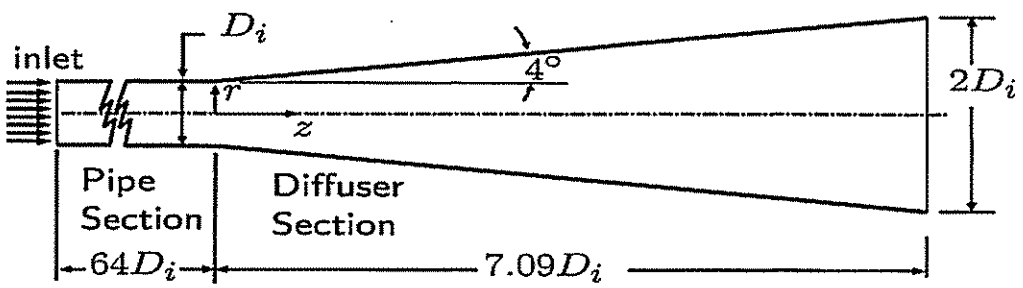

Figure 1: *Conical diffuser geometry and coordinate system*

a wall-function, low Reynolds number k-ε with no correction for streamwise pressure gradient, and low Reynolds number k-ε with a pressure gradient parameter to capture the effects of streamwise pressure curvature on the turbulent structure. The results show that low Reynolds number model with pressure gradient parameter gives better prediction of the skin friction distribution than the low Reynolds number model without pressure gradient parameter or when a wall-function is used.

Cho and Fletcher [7] applied a k-ε model and an algebraic Reynolds stress model (ASM) model with wall-function to predict the experimental results of Azad and Kassab [3] at Re = 115,000. The ASM model gave a slightly better prediction of the mean velocity profile and Reynolds shear stress than the k-ε model. However, both models substantially over predicted the friction velocity in the exit section of the diffuser, and fail to predict the correct levels of the turbulence kinetic energy and Reynolds shear stress.

In the present study, CFX-TASCflow together with the low Reynolds number k-ε of Launder and Spalding [8], the standard k-ω [9], the k-ω BSL of Menter [10], the k-ω non-linear algebraic Reynolds stress model of Gatski and Speziale [11], and the ε-based second moment closure (SMC-LRR-IP) of Launder *et al.* [12] are applied to compute the experimental results of Singh [1] and Kassab [2] at Re = 69,000 and 115,000, respectively. The datasets available for comparison include mean velocity profiles, static pressure, friction velocity, skin friction, turbulence kinetic energy, and Reynolds shear stress in the fully developed section of the inlet pipe and at various stations in the diffuser.

2.0 MATHEMATICAL MODEL

2.1 Governing Equations

The governing equations for steady, incompressible flow may be written in tensor form as follows:

$$\frac{\partial U_j}{\partial x_j} = 0 \tag{1}$$

$$\rho U_j \frac{\partial U_i}{\partial x_j} = -\frac{\partial P}{\partial x_i} + \frac{\partial}{\partial x_j}\left(\mu \frac{\partial U_i}{\partial x_j} - \rho \overline{u_i u_j} \right) \tag{2}$$

where $\overline{u_i u_j}$ is the Reynolds stress tensor and ρ is the mean density. The turbulent models used to compute the Reynolds stress tensor are discussed in the next section.

2.2 Turbulence Models

The five turbulence models used in this study are low Reynolds number k-ε of Launder and Spalding [8], the standard linear-eddy-viscosity k-ω model of Wilcox [9], hereafter referred to as k-ω, the k-ω BSL of Menter [10], the k-ω based non-linear algebraic Reynolds stress (k-ω ASM)

of Gatski and Speziale [11], and the ε-based second moment closure (SMC-LRR-IP) proposed by Launder *et al.* [12]. The equations solved for the k-ε model are given in equations 3 and 4.

$$\rho\frac{\partial\left(U_j k\right)}{\partial x_j}=\frac{\partial}{\partial x_j}\left(\left(\mu+\frac{\mu_t}{\sigma_k}\right)\frac{\partial k}{\partial x_j}\right)+P_k-\rho\varepsilon \tag{3}$$

$$\rho\frac{\partial\left(U_j \varepsilon\right)}{\partial x_j}=\frac{\partial}{\partial x_j}\left(\left(\mu+\frac{\mu_t}{\sigma_\varepsilon}\right)\frac{\partial \varepsilon}{\partial x_j}\right)+\frac{\varepsilon}{k}\left(c_{\varepsilon 1}P_k-\rho c_{\varepsilon 2}\varepsilon\right) \tag{4}$$

where $c_{\varepsilon 1}$, $c_{\varepsilon 2}$, σ_k, σ_ε, and c_μ are constants with values 1.44, 1.92, 1.0, 1.3 and 0.09 respectively. The two layer model (which is referred to as low-Reynolds number model in CFX-TASCflow v2.12) was used. This model employed the standard k-ε model far away from the wall region and one-equation model in the near wall region. The dissipation rate of turbulent kinetic energy, ε, and eddy viscosity are given as:

$$\varepsilon=\frac{k^{3/2}}{l_t f_\varepsilon} \tag{5}$$

$$\mu_t=\rho C_\mu \sqrt{k} l_t f_\mu \tag{6}$$

where the eddy length scale, $l_t=\kappa n / C_\mu^{3/4}$, κ is von Karman constant, n is the distance from the solid wall and, f_ε and f_μ are damping functions computed from the following expressions proposed by Yap [13]:

$$f_\varepsilon=1-\exp\left(-R_n / A_\varepsilon\right) \tag{7}$$

$$f_\mu=1-\exp\left(-R_n / A_\mu\right) \tag{8}$$

A_ε and A_μ are constants with values 3.8 and 63, respectively, and $R_n=\rho n\sqrt{k}/\mu$.

The standard k-ω model developed by Wilcox [9] solves equations (9) and (10), respectively, for k and ω:

$$\rho\frac{\partial\left(U_j k\right)}{\partial x_j}=\frac{\partial}{\partial x_j}\left(\left(\mu+\frac{\mu_t}{\sigma_k}\right)\frac{\partial k}{\partial x_j}\right)+P_k-\rho\beta^* k\omega \tag{9}$$

$$\rho\frac{\partial\left(U_j \omega\right)}{\partial x_j}=\frac{\partial}{\partial x_j}\left(\left(\mu+\frac{\mu_t}{\sigma_\omega}\right)\frac{\partial \omega}{\partial x_j}\right)+\alpha\frac{\omega}{k}P_k-\rho\beta\omega^2 \tag{10}$$

where $\omega=\varepsilon/k$ is the specific dissipation rate. The eddy-viscosity, μ_t, Reynolds stress tensor $\overline{u_i u_j}$ and production term, P_k are computed from the following expressions:

$$\mu_t = \rho C_\mu (k/\omega) \tag{11}$$

$$-\rho\overline{u_i u_j} = \mu_t\left(\frac{\partial U_i}{\partial x_j}+\frac{\partial U_j}{\partial x_i}\right)-\rho\frac{2}{3}\delta_{ij}k \tag{12}$$

$$P_k = \mu_t\left(\frac{\partial U_i}{\partial x_j}+\frac{\partial U_j}{\partial x_i}\right)\frac{\partial U_i}{\partial x_j} \tag{13}$$

The values of the model coefficients are as follows: $\sigma_k = 2$, $\sigma_\omega = 2$, $\alpha = 5/9$, $\beta = 0.075$, $\beta^* = 0.09$, and $C_\mu = 0.09$. The equations solved for the BSL model are given in Equations (14) and (15).

$$\rho\frac{\partial\left(U_j k\right)}{\partial x_j} = \frac{\partial}{\partial x_j}\left(\left(\mu+\frac{\rho C_\mu k}{\sigma_{k1}\omega}\right)\frac{\partial k}{\partial x_j}\right)+P_k-\beta^*\rho k\omega \tag{14}$$

$$\rho\frac{\partial\left(U_j \omega\right)}{\partial x_j} = \frac{\partial}{\partial x_j}\left(\left(\mu+\frac{\rho C_\mu k}{\sigma_{\omega 1}\omega}\right)\frac{\partial \omega}{\partial x_j}\right)+\alpha_2\frac{\omega}{k}P_k-\rho\beta_1\omega^2+\left(1-F\right)2\rho\sigma_{\omega 1}\frac{1}{\omega}\frac{\partial k}{\partial x_j}\frac{\partial \omega}{\partial x_j} \tag{15}$$

where σ_{k1}, $\sigma_{\omega 1}$, α_1, and β_1 are constants with values 1, 0.856, 0.44, and 0.0828, respectively. All the other constants have their usual meanings and the blending function, F, ($F = tanh(arg^4)$) with $\arg = \min\left(\max\left(\frac{\sqrt{k}}{\beta^*\omega y};\frac{500\nu}{y^2\omega}\right);\frac{4\rho\sigma_{\omega 1}k}{CD_{k\omega}y^2}\right)$; $CD_{k\omega} = \max\left(2\rho\sigma_{\omega 1}\frac{1}{\omega}\frac{\partial k}{\partial x_j}\frac{\partial \omega}{\partial x_j}, 1.0\times E^{-10}\right)$ where y is the distance to the nearest surface. For the k-ω based algebraic stress model, the same k and ω equations, (Equations 5 and. 6) are solved but in this case, $\mu_t = \rho C^*_\mu (k/\omega)$, and the model constants have the following values: $\sigma_k = 1.4$, $\sigma_\omega = 2.0$, $\alpha = 0.5467$, $\beta = 0.83$, $\beta^* = 1.0$ and $C^*_\mu = 0.088$. The Reynolds stress tensor is computed from the following expression:

$$\rho u_i u_j = \frac{2}{3}\rho k\delta_{ij}-2\mu_t^*\left[\left(S_{ij}-\frac{1}{3}S_{kk}\delta_{ij}\right)+\frac{\lambda_1}{\omega}\left(S_{ik}\Omega_{kj}+S_{jk}\Omega_{ki}\right)-\frac{\lambda_5}{\omega}\left(S_{ik}S_{kj}-\frac{1}{3}S_{kl}S_{kl}\delta_{ij}\right)\right] \tag{16}$$

with μ^*_t, C^*_μ, mean rate-of-strain S_{ij}, the mean-vorticity tensor Ω_{ij}, and the model constants given as:

$\mu_t^* = \rho C_\mu^*(k/\omega)$, $C_\mu^* = \frac{3(1+\eta^2)\lambda_1}{3+\eta^2+6\eta^2\beta^2+6\beta^2}$, $S_{ij} = \frac{1}{2}\left(\frac{\partial U_i}{\partial x_j}+\frac{\partial U_j}{\partial x_i}\right)$, $\Omega_{ij} = \frac{1}{2}\left(\frac{\partial U_i}{\partial x_j}-\frac{\partial U_j}{\partial x_i}\right)$,

$\eta^2 = \left(\lambda_2/\omega^2\right)\left(S_{ij}S_{ij}\right)$, $\beta^2 = \left(\lambda_3/\omega^2\right)\left(\Omega_{ij}\Omega_{ij}\right)$, $\lambda_1 = \left(4/3-A_2\right)(g/2)$, $\lambda_2 = \left(2-A_3\right)^2(g^2/4)$,

$\lambda_3 = \left(2-A_4\right)^2(g^2/4)$, $\lambda_4 = \left(\frac{2-A_4}{2}\right)g$, $\lambda_5 = \left(2-A_3\right)g$, and $g = \frac{1}{(A_1/2)+A_5-1}$. The coefficients have the following values: $A_1 = 3$; $A_2 = 0.8$; $A_3 = 1.75$, $A_4 = 1.31$; and $A_5 = 2$. A

near-wall treatment which automatically switches from wall-function to a low-Reynolds number formulation as the grid is refined was employed for both k-ω based models.

For the second moment closure, the Reynolds stress tensor $\overline{u_i u_j}$ is obtained from its exact differential equation. In the present work, the pressure-strain correlation developed by Launder *et al.* (LRR-IP) [12] is adopted. The diffusion term is modelled following the proposal of Daly and Harlow [14]. The modelled equations are as follows:

$$U_k \frac{\partial}{\partial x_k}\left(\rho\overline{u_i u_j}\right) = -\rho\overline{u_k u_i}\frac{\partial U_j}{\partial x_k} - \rho\overline{u_k u_j}\frac{\partial U_i}{\partial x_k} + \frac{\partial}{\partial x_k}\left[\left(c_s \rho \frac{k}{\varepsilon}\overline{u_k u_l} + \mu\delta_{kl}\right)\frac{\partial \overline{u_i u_j}}{\partial x_l}\right] - c_1\frac{\varepsilon}{k}\left(\rho\overline{u_i u_j} - \frac{2}{3}\rho k\delta_{ij}\right) - c_2\left(P_{ij} - \frac{2}{3}\delta_{ij}P_k\right) - \frac{2}{3}\rho\varepsilon\delta_{ij} \tag{17}$$

$$U_k \frac{\partial(\rho\varepsilon)}{\partial x_k} = \frac{\partial}{\partial x_k}\left(\left(c_\varepsilon \rho \frac{k}{\varepsilon}\overline{u_k u_i} + \mu\delta_{kl}\right)\frac{\partial\varepsilon}{\partial x_l}\right) + \frac{\varepsilon}{k}\left(c_{\varepsilon 1}P_k - c_{\varepsilon 2}\rho\varepsilon\right) \tag{18}$$

The values of the model constants are: $c_1 = 1.8$, $c_2 = 0.6$, $c_s = 0.22$, $c_{\varepsilon 1} = 1.45$, $c_{\varepsilon 2} = 1.9$, and $c_\varepsilon = 0.18$. This model will be denoted as SMC-LRR in the subsequent sections. A wall-function approach is employed for the near-wall treatment because it is the only wall treatment available for SMC-LRR in CFX-TASCflow version 2.12. As would be mentioned later in Section 3.2, one quarter of the full domain was chosen for the computations.

2.3 Boundary Conditions

The boundary conditions for the diffuser include the specification of the velocity at the inlet of the pipe section, an outflow boundary at the exit plane of the diffuser, and no-slip boundary condition on the wall surfaces. The outflow boundary condition consists of setting the average pressure at the entire outlet area to a reference value of zero. Symmetry conditions were applied at the horizontal and vertical boundary planes of the domain shown in Figure 2.

The computational domain includes a pipe section of length $64D_i$ before the diffuser section. For flow predictions of the Singh [1] dataset, a bulk velocity of U_b = 10.5 m/s was specified at the pipe inlet, producing a Reynolds number based on U_b and D_i = 0.1016 m of 69,000. The turbulence intensity I = 10% was specified and k was computed from $k = 1.5I^2U^2_b$. The turbulent intensity value was obtained from experimental data for the fully developed section of the inlet pipe. The dissipation rate was computed from the turbulent viscosity ratio (μ_t/μ) using $\varepsilon = C_\mu \rho k^2/\mu_t$ and $\mu_t/\mu = 1000I$. The flow in the pipe was fully-developed at the inlet to the diffuser section.

In the case of the Kassab [2] dataset, a bulk velocity of U_b = 18.06 m/s was specified at the pipe inlet, producing a Reynolds number based on U_b and D_i = 0.1016 m of 115,000. At the pipe inlet, a turbulence intensity values of I = 5.164% was specified. The dissipation rate of k at the inlet was computed from $\varepsilon = k^{1.5}/L_\varepsilon$, where L_ε is the eddy length scale. A value of L_ε = 0.0339

m was used. The same conditions were specified for the k-ω model, and ω was computed from $\omega = \varepsilon / k$. The above specified values for both turbulence intensity and eddy length scale were chosen from the experimental data for the fully developed section of the inlet pipe.

3.0 NUMERICAL SOLUTION

3.1 Solution Method

The numerical solution of the equations of motion was obtained using CFX-TASCflow, version 2.12. CFX-TASCflow uses a finite volume method (Patankar [15]), but is based on a finite element approach of representing the geometry. Cartesian velocity components were used on a non-staggered, structured, multi-block grid. Mass conservation discretisation on the non-staggered grid is an adaptation of earlier techniques (Rhie and Chow [16]; Prakash and Patankar [17]; Schneider and Raw [18]). In the discretisation, a standard finite element derivative approximation via shape functions is used for diffusion terms. Advection term discretisation uses a physical advection correction with a mass weighted modification to the skew upwind differencing scheme (Raithby [19]), adapted from earlier proposed schemes (Schneider and Raw [18]; Ronel and Baliga [20]; Lillington [21]; Huget [22]; and Raw [23]). All the simulations presented here were based on the Mass Weighted Scheme as the advection discretisation scheme.

The discretised mass and momentum conservation equations are fully coupled and solved simultaneously using additive correction multigrid to accelerate convergence. Single precision was used in the computations and solutions were considered converged when the normalised sum of the absolute dimensionless residuals of the discretised equations was less than 1.0×10^{-5} for the Singh [1] dataset and 1.0×10^{-5} for the Kassab [2] dataset.

3.2 Computational Mesh

A single block structured computational mesh representing the entire domain shown in Figure 1, was created using CFX Build version 4.4 and then imported into CFX-TASCflow. Because an axisymmetric version of CFX-TASCflow was not available, a segment representing one quarter of the diffuser cross-section was used in the mesh generation. Figure 2 shows an example of a mesh used for the cross-section of the quarter segment. In this plane, the mesh consists of three regions: a rectangular region near the centre of the pipe, and two regions between the rectangular region and the arc representing the pipe wall, and they are separated by a line from the corner of the rectangular region to the arc. The grid was uniformly spaced in the rectangular region, and contracted geometrically towards the wall outside that region. In the axial direction, uniform grid spacing was used, and the radius of the quarter-segment increased in the diffuser section.

A number of grid meshes were used to determine grid independence of the solutions. A typical number of nodes in the streamwise direction of the pipe section was 530. The transverse grid spacing was refined towards the wall. The same distribution was used in the pipe and diffuser sections. The grid independence tests on the diffuser section were conducted using grids made up of 39 x 35, 69 x 75, 99 x 115, respectively for Singh [1] and 30 x 30, 55 x 55, 85 x 85, respectively for Kassab [2], in the wall- normal and stream-wise directions, respectively. Based on centreline velocity and pressure coefficient, the maximum differences between the coarse and medium grids were 1.8 %. In terms of typical local velocity profiles examined at two axial locations, the maximum percentage changes were 1.1%. The corresponding differences between the medium and fine grids were 0.2% and 0.3% respectively. Based on these tests, the medium

grid was used for all the models. For the SMC-LRR, a wall-function approach was employed because it is the only option available in CFX-TASCflow 2.12. Preliminary computations performed using both the standard and scalable wall-function for SMC-LRR shows about 5% difference between quantities at 3 points in the domain. The SMC-LRR results presented in this paper are based on the scalable wall-function.

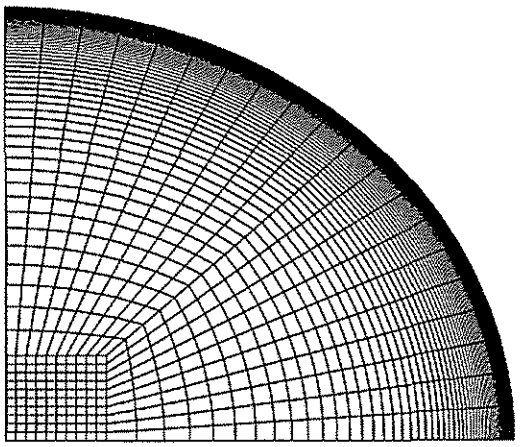

Figure 2: End view of an example conical diffuser computational grid

4.0 RESULTS AND DISCUSSION

4.1 Comparison of k-ε and k-ω based models with Singh [1] Experimental Data

Here, two k-ω based models (standard k-ω and k-ω –BSL) and low-Reynolds number k-ε model were used to predict the flow corresponding to the Singh [1] dataset. The results from the two k-ω based models were identical, and therefore only the standard k–ω results will be presented. A comparison of mean velocity profiles and distributions of the friction velocity and pressure coefficient at various stations was performed. Although numerical solutions were obtained for Cartesian velocity components, results are presented here in terms of the r-z coordinates shown in Figure 1.

Figure 3 shows radial distributions of Ur at stations z/D_i = -0.25 (pipe section) and 2.32, 5.48, 6.84 (diffuser section). As expected, both models predicted the mean velocity in the fully developed section of the inlet pipe reasonably well. The k-ω results are in excellent agreement with the experimental data in the early section of the diffuser. However, the agreement between the k-ω results and experiment data deteriorated in the core regions of stations close to the diffuser exit. The results from the k-ε model are less accurate compared with the k-ω results.

A comparison of the calculated and measured friction velocity $U_\tau = (\tau_w / \rho)$, where τ_w is wall shear stress, is presented in Figure 4. The results from the k-ω model are in excellent agreement with the experimental data, falling within the measurement uncertainty of ±10%. The k-ε model under estimated the friction velocity in the diffuser. As mentioned in the introduction, Lai *et al* [8] applied various versions of k-ε model to calculate turbulent flow in the same conical diffuser but at a higher Reynolds number. Their results show that U_τ values calculated from application of wall function, or low Reynolds number k-ε with no pressure correction term deviate

significantly from the experimental data. Wilcox [24] observed that the predicted values of skin friction coefficient in mild, moderate and strong adverse pressure gradients from k-ω model are within 2.4% and 5.9% of measured values On the other hand, the differences between measured and computed values from k-ε model for the same flows varied from 27% to 42%.

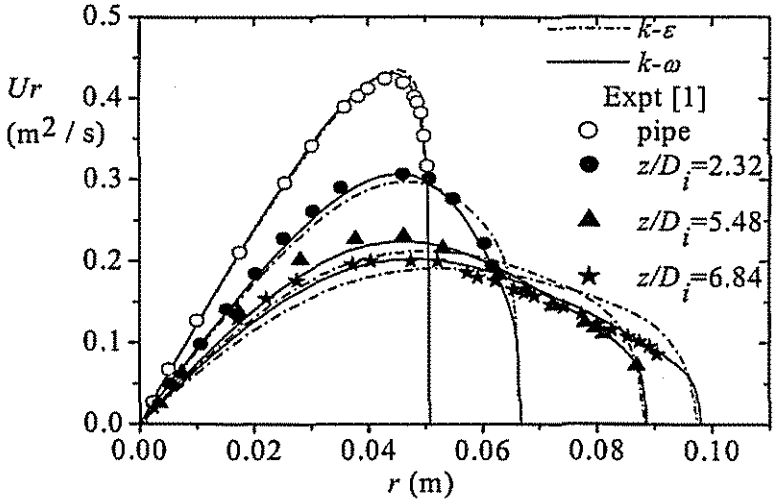

Figure 3: *Ur versus r curves for mean velocity profiles at various stations in the inlet pipe and diffuser*

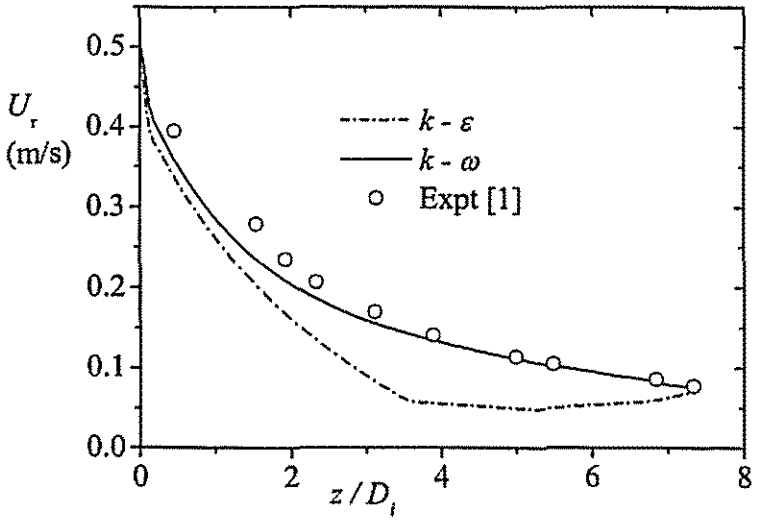

Figure 4: *Comparison of computed and measured frictional velocity for the conical diffuser*

Figure 5 shows the distribution of the wall static pressure recovery coefficient, C_p ($C_p = \left(P_s - P_{s(ref)}\right)/(0.5\rho U_b^2)$), where $P_{s(ref)}$ is P_s at z/D_i = -0.25. The results obtained from both models were in good agreement with experimental data. A similar good agreement between calculated and measured values of pressure distribution was noted by Lai *et al* [6]. The general inference from the above discussion is that the k-ω model did slightly better than the k-ε model. This may be attributed to the ability of the k-ω model to accounts for the effects of streamwise pressure gradients [9].

4.2 Comparison of k-ω based and SMC-LRR models with Kassab [2] Experimental Data

In this section, we compare numerical results obtained using the standard k-ω model, the k-ω ASM model and the SMC-LRR model to the experimental data of Kassab [2]. Figure 6 compares the numerical results of the mean velocity profiles with experimental data at selected stations (z/D_i = 1.77, 4.13, 6.5) in the diffuser section. In this figure, the half-power law proposed by Schofield [25] is used. Here, y_w is the wall-normal distance measured from the diffuser wall and $\delta^* = R - (D_i/2)(U_b/U_c)^{1/2}$, where R is the local radius and U_c is the local centreline velocity. The results shown in Figure 6 demonstrate that all the models predict the mean velocity reasonably well in regions away from the wall. However, the performance of the three models close to the wall varies. For example, the predictions from the k-ω are in excellent agreement with measured values at all stations while the k-ω ASM model under-predicted the near-wall region of the mean velocity profiles at stations z/D_i = 4.13 and 6.5. The SMC-LRR model, on the other hand, give values that are significantly lower than measured values at z/D_i = 1.17 and 4.13, but in good agreement with measured values at the exit section of the diffuser. The shape of the velocity profiles is consistent with prior measurements obtained in strong adverse pressure gradients where the flow is near separation.

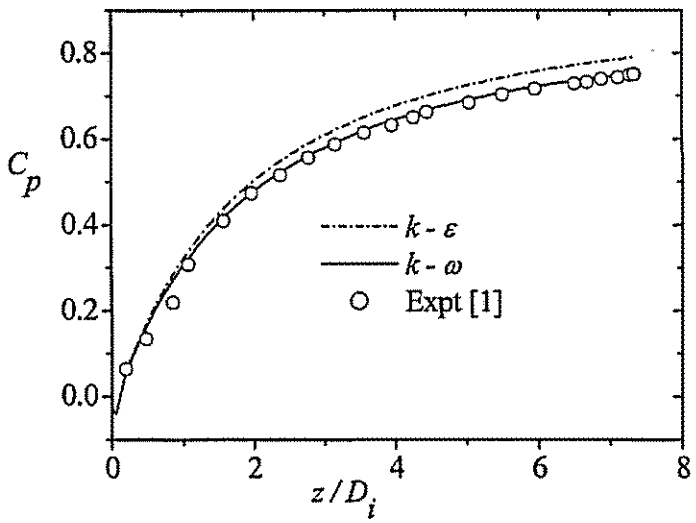

***Figure 5:** Comparison of computed and measured pressure coefficient for the conical diffuser*

Figure 7 shows the distribution of the local friction velocity, U_τ along the walls of the feed pipe and the diffuser. The numerical values obtained by Lai *et al.* [6] with a wall-function are also shown in Figure 7. The figure shows that the U_τ values obtained from the low-Reynolds number k-ω models (particularly the standard k-ω model) are in good agreement with measured values. The U_τ values from the SMC-LRR and prior results of Lai *et al.* [6], on the other hand, are significantly higher than the experimental values.

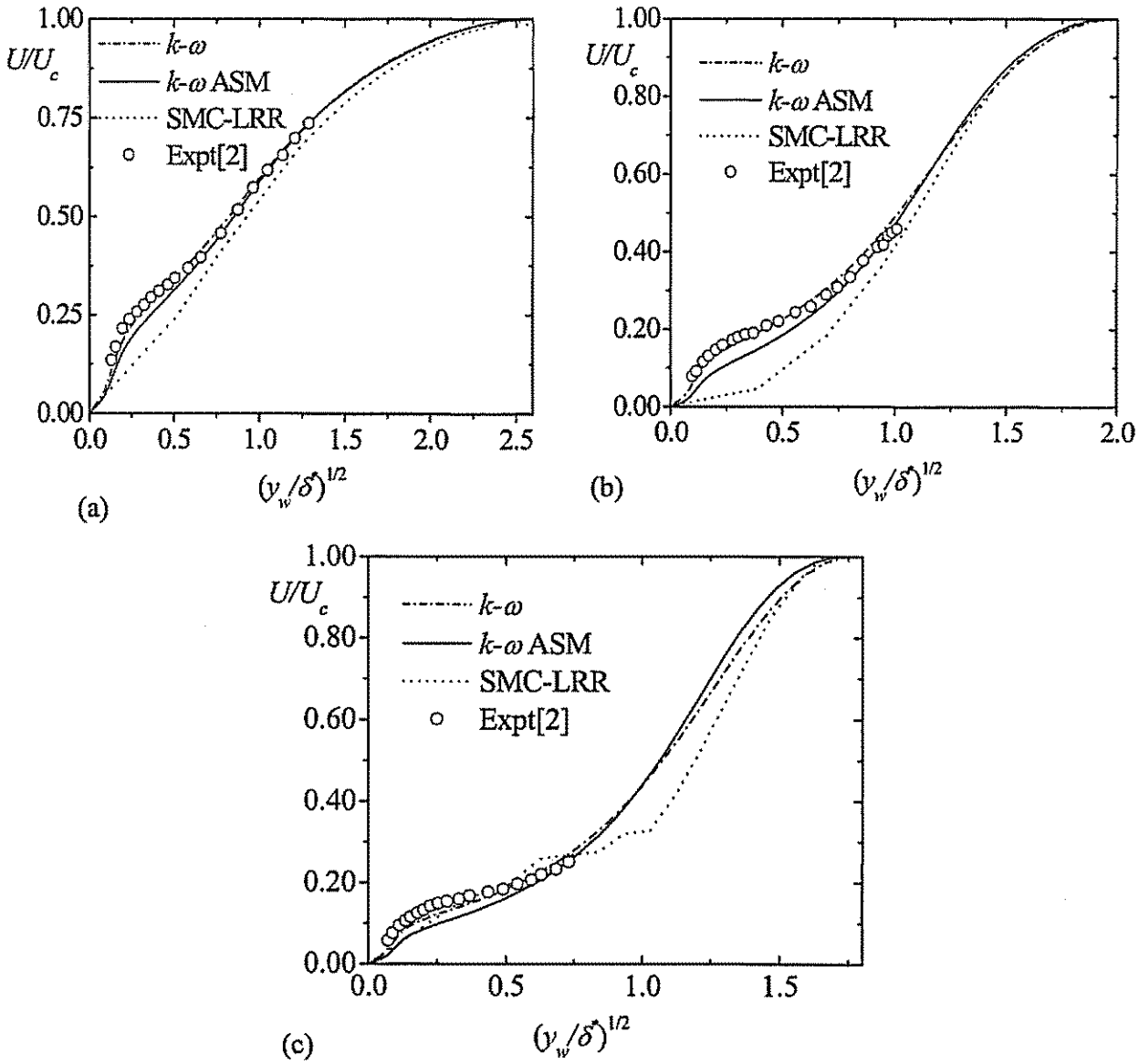

Figure 6: *Radial distribution of mean velocity at* z/D_l = (a) 1.77, (b) 4.13 and (c) 6.5

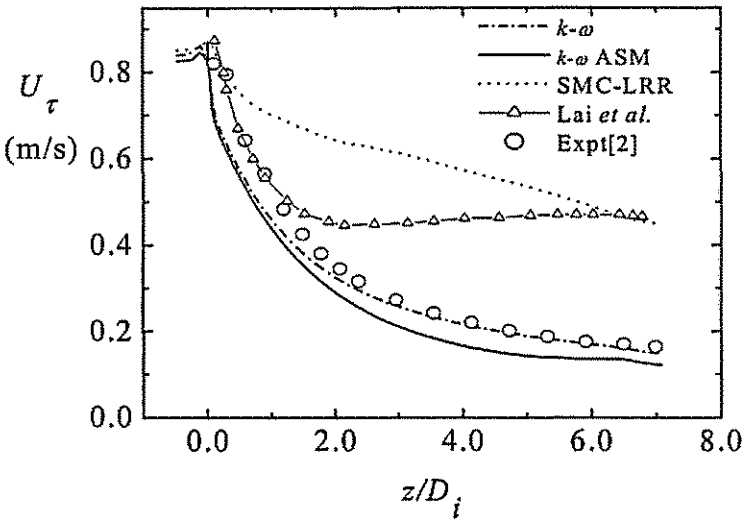

***Figure 7**: Axial distribution of friction velocity*

The discrepancy between these numerical results and the experiment data increases as the exit section of the diffuser is approached. It should be noted that all the models, including SMC-LRR, predicted the correct value of U_τ in the fully developed section of the inlet pipe where no adverse streamwise pressure gradient exists. The higher U_τ values obtained from the present SMC-LRR and Lai *et al.* [6] in the diffuser section demonstrate that ε-based models are not as suitable as ω-based models in predicting the skin friction coefficient in adverse pressure gradient turbulent flows.

The numerical and measured values of the static pressure coefficient, C_p, as defined earlier on with $P_{s(ref)}$ taken as P_s at z/D_i = -1.0 along the diffuser are compared in Figure 8. The values obtained from the three models are in good agreement with measured values as expected. This suggests that C_p in a conical diffuser can be correctly calculated irrespective of the near-wall treatment or whether a transport equation is solved for ε or ω.

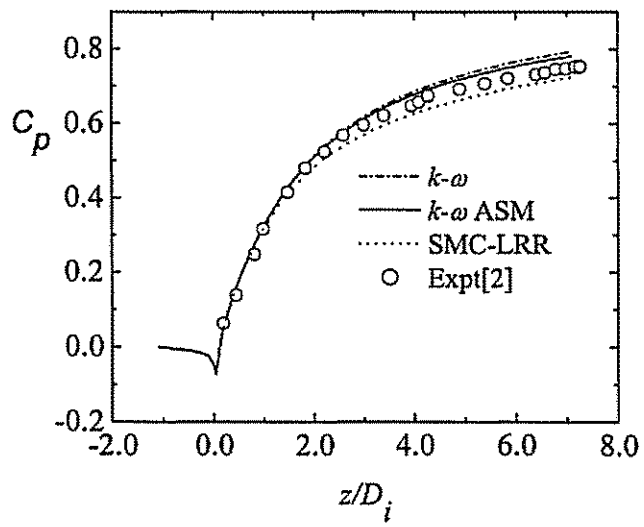

***Figure 8**: Axial distribution of pressure coefficient*

The distribution of the turbulence kinetic energy at z/D_i = 1.77, 4.13 and 6.5 are shown in Figure 9. The numerical results of Cho and Fletcher [7] using ASM model (denoted as AASM) are also shown for comparison. It should be noted that in this and subsequent figures, r = 0 corresponds to the centreline and not the diffuser wall. All models (both present and past) predicted the correct trends of the kinetic energy. The present models give reasonable prediction in the near-wall region but substantially under-predicted the experimental data in the intermediate and core regions. Overall, the SMC-LRR did slightly better than the k-ω based models in the core region. As shown in Figure 9 (b) and (c), the results of Cho and Fletcher [7] are in better agreement with experiment at z/D_i = 1.77 and 4.13 than the present results.

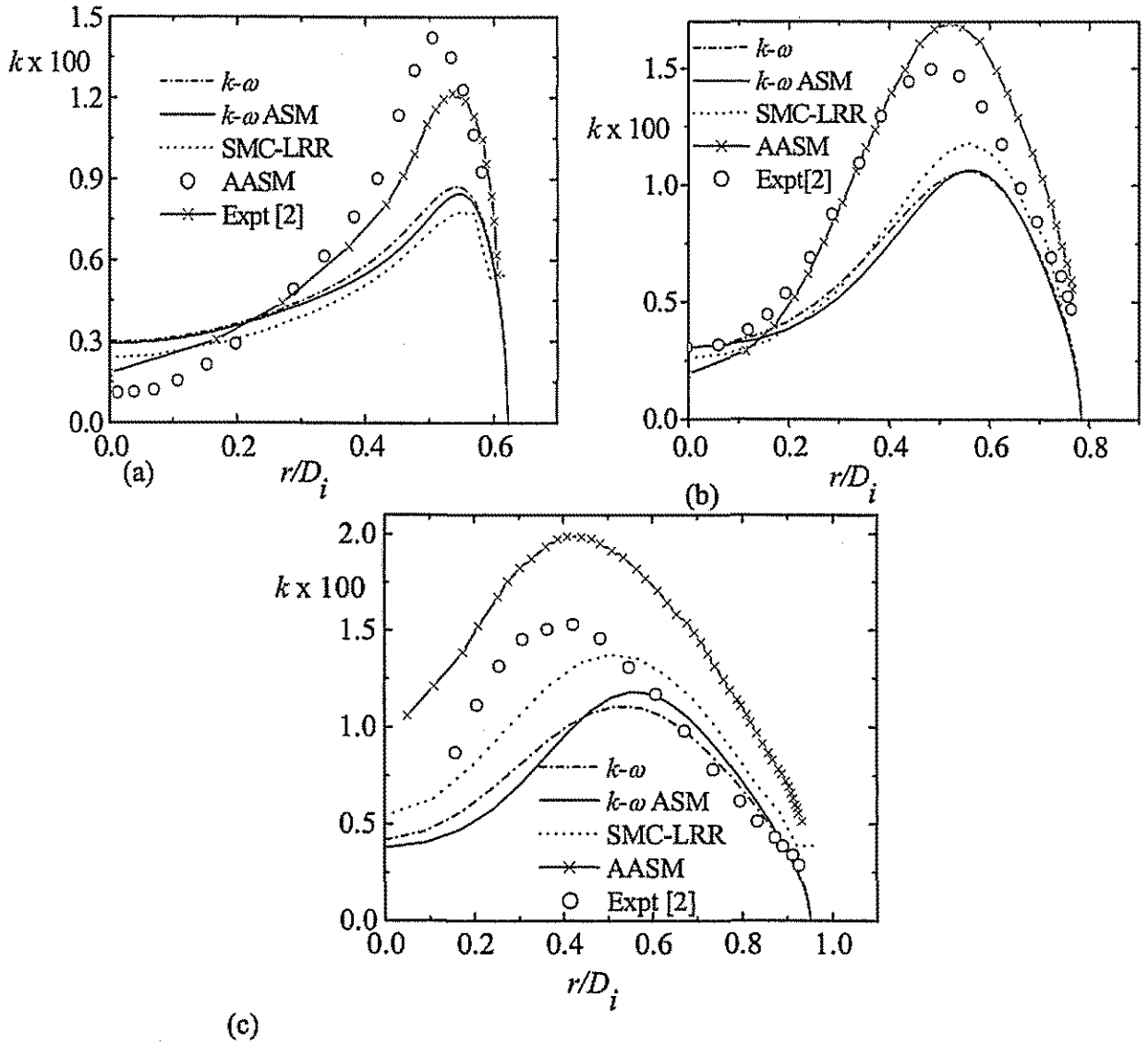

***Figure 9**: Radial distribution of turbulent kinetic energy at z/D_i = (a) 1.77, (b) 4.13 and (c) 6.5*

Figure 10 shows the distribution of the Reynolds shear stress *(uv)* at three axial stations. The models used in the present study predicted the trend and peak value at all stations reasonably well. The numerical results of Cho and Fletcher [7], on the other hand, significantly over-predicted the level of *uv*, particularly in the near-wall region. Cho and Fletcher [7] attribute the over prediction of the Reynolds shear stress in the downstream region to the presence of the dissipation equation which produces length scales that are too high in near-separating flows. They also indicated that retaining dissipation in full Reynolds stress turbulence models would show no significant improvement in the prediction.

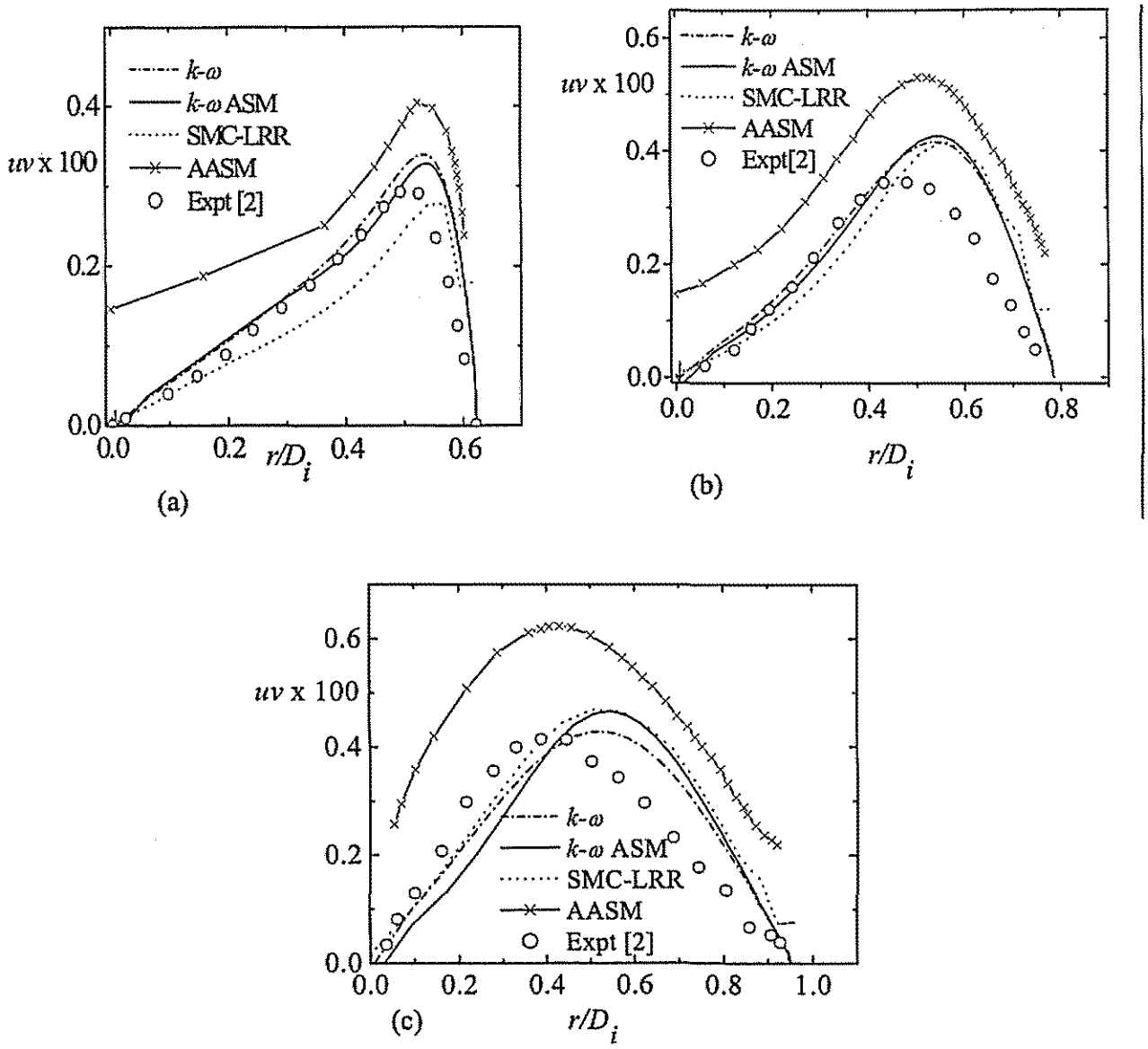

Figure 10: *Radial distribution of Reynolds shear stress at z/D_i = (a)* 1.77, *(b)* 4.13 and *(c)* 6.5

5.0 CONCLUSION

CFX-TASCflow together with various near-wall turbulence models was used to predict near-separating turbulent flow in a conical diffuser. The present results compare favourably well with prior computations performed using in-house CFD codes with similar turbulence models and near-wall treatments.

The results presented in this paper demonstrate that the static pressure obtained from all the turbulence models, irrespective of level of complexity, transport equations solved, and near-wall treatment, are in excellent agreement with experiment. However, the ω-based models gave significantly more accurate prediction of the wall shear stress or skin friction coefficient in adverse pressure gradient than the ε-based models.

A comparison between numerical and measured values of the turbulence kinetic energy and Reynolds shear stress revealed that application of the specific second moment closure employed in the present study does not show any marked improvement in comparison to the lower level turbulence models. Thus, on balance, in this application a low Reynolds number eddy viscosity k-ω model is more suitable for predicting turbulent diffuser flows than a second moment closure model with a wall-function.

REFERENCES

[1]. Singh, R. K., The Characteristics of Turbulent Flow in a Conical Diffuser, PhD Thesis, University of Manitoba, 1995.

[2]. Kassab, S. Z., Turbulence Structure in Axisymmetric Wall-Bounded Shear Flow, PhD Thesis, University of Manitoba, Winnipeg, Canada, 1986.

[3]. Azad, R. S., and Kassab, S. Z., Turbulent Flow in a Conical Diffuser: Overview and Implications, Physics of Fluids, **A 1** (3), 564-573, 1989.

[4]. Arora, S. C. and Azad, R. S., Applicability of the isotropic vorticity theory to an adverse pressure gradient flow, Journal of Fluid Mechanics, **97**, part 2, 385- 404, 1980.

[5]. Trupp, A. C, Azad, R. C., and Kassab, S. Z., Near-Wall Velocity Distributions within a Straight Conical Diffuser, Experiments in Fluids, **4**(8), 319-331,1986.

[6]. Lai, Y. G., So, R. M., and Hwang, B. C., Calculation of Planar and Conical Diffuser Flows, AIAA, **27**(5): 542-548, 1988.

[7]. Cho, Nam-Hyo and Fletcher, C. A. J., Computation of Turbulent Conical Diffuser Flows Using a Non-orthogonal Grid System, Computers and Fluids, **19** (3/4): 347-361, 1991.

[8]. Launder, B. E. and Spalding, D. B., The Numerical Computation of Turbulent Flows, Comp. Meth. Appl. Mech. Eng, **3**, 269-289, 1974.

[9]. Wilcox, D. C., Multiscale Model for Turbulent Flows, AIAA Journal, **26**, 1311-1320, 1988.

[10]. Menter, F. R., Two-Equation Eddy-Viscosity Turbulence Models for Engineering Applications, AIAA Journal, **32** (8), 37-40, 1994.

[11]. Gatski, T. B. and Speziale, C. G., On Explicit Algebraic Stress Models for Complex Turbulent Flows, Journal of Fluid Mechanics, **254**, 59-78, 1993.

[12]. Launder, B. E., Reece, G. J., and Rodi, W., Progress in the Development of a Reynolds Stress Turbulence Closure, Journal of Fluid Mechanics, **68**, 537-566,1975.

[13]. Yap, C. R., Turbulent Heat and Momentum Transfer in Recirculating and Impinging Flows. Doctoral Thesis, University of Manchester, Manchester, England, U.K., 1987.
[14]. Daly, B. J. and Harlow, F. H., Transport Equations in Turbulence, Physics of Fluids, **13**, 2634-2649, 1970.
[15]. Patankar, S.V., Numerical Heat Transfer and Fluid Flow, Hemisphere Publishing Corporation, New York, 1980.
[16]. Rhie, C. M. and Chow, W. L., Numerical Study of the Turbulent Flow Past an Airfoil with Trailing Edge Separation, AIAA Journal, **21**(11), 1525-1532, Nov. 1983.
[17]. Prakash, C. and Patankar, S. V., A Control Volume-Based Finite-Element Method for Solving the Navier-Stokes Equations using Equal-Order Velocity-Pressure Interpolation, Numerical Heat Transfer, **8**, 259-280, 1985.
[18]. Schneider, G. E. and Raw, M. J., A Skewed, Positive Influence Coefficient Upwinding Procedure for Control-Volume-Based Finite Element Convection-Diffusion Computation, Numerical Heat Transfer, **8**, 1-26, 1986.
[19]. Raithby, G. D., Skew Upstream Differencing Schemes for Problems Involving Fluid Flow, Computational Methods for Applied Mechanical Engineering, **9**, 153-164, 1976.
[20]. Ronel, J. and Baliga, B. R., A Finite Element Method for Unsteady Heat Conduction in Materials with or without Phase Change, ASME Paper 79-WA-HT-54, American Society of Mechanical Engineers Winter Annual Meeting, New York, U.S.A., 1979.
[21]. Lillington, J. N., A Vector Upstream Differencing Scheme for Problems in Fluid Flow Involving Significant Source Terms in Steady-State Linear Systems, Int. J. Numerical Methods in Fluids, **1**, 3-16, 1981.
[22]. Huget, R. G., The Evaluation and Development of Approximation Schemes for the Finite Volume Method, Ph.D. Thesis, University of Waterloo, Waterloo, Canada, 1985.
[23]. Raw, M. J., A New Control-Volume-Based Finite Element Procedure for the Numerical Solution of the Fluid Flow and Scalar Transport Equations, Ph.D. Thesis, University of Waterloo, Waterloo, Ontario, Canada, 1985.
[24] Wilcox, D. C., Turbulence Modelling for CFD, 2nd Edition, Birmingham Press, Inc. San Diego, Carlifonia, 2004.
[25]. Schofield, W. H., Equilibrium Boundary Layers in Moderate to Strong Adverse Pressure Gradients, Journal of Fluid Mechanics, **113**, 91-122, 1981.